15 Many-Body Localization

Julian Léonard
TU Wien
Stadionallee 2, 1020 Wien

Contents

E. Pavarini and E. Koch (eds.)
Correlations and Phase Transitions
Modeling and Simulation Vol. 14
Forschungszentrum Jülich, 2024, ISBN 978-3-95806-751-6
http://www.cond-mat.de/events/correl24

1 Introduction

An important class of systems that give rise to new types of order are non-equilibrium systems. An isolated quantum system that is brought far from equilibrium typically relaxes to a state which is locally described by a thermal ensemble. Although the initial global purity persists, the coupling between any subsystem and remainder of the system mimics the contact with a bath, which drives local thermalization. Few exceptions to this paradigm are known. Disorder, for example, can bring non-equilibrium systems into a many-body-localized (MBL) state where thermalization is absent. In those systems, no local order parameter or symmetry breaking is known, and the role of fluctuations at the transition between thermal and localized states remains to be understood. The distinctive feature of the MBL phase, which may be associated with the order in the system, is the evolution of the non-local entanglement, which leads to a characteristic scaling of the entanglement entropy that is logarithmic in time.
In this lecture we will review experimental work on many-body localization, following the path of three key publications. We first discuss the many-body localized state itself, realized as a disordered, isolated quantum system of a controllable number of atoms in an optical lattice. We will then discuss the critical behavior at intermediate disorder and explore the boundary between the classical dynamics at weak disorder,and the quantum dynamics at strong disorder. Finally, we will talk about the robustness of MBL against a thermal inclusion, and quantum avalanches as a possible instability of MBL at long evolution times. The lecture notes have been published as [1–3].

2 Many-body localization

An interacting quantum system that is subject to disorder may cease to thermalize due to localization of its constituents, thereby marking the breakdown of thermodynamics. The key to our understanding of this phenomenon lies in the system's entanglement, which is experimentally challenging to measure. We realize such a many-body-localized system in a disordered Bose-Hubbard chain and characterize its entanglement properties through particle fluctuations and correlations. We observe that the particles become localized, suppressing transport and preventing the thermalization of subsystems. Notably, we measure the development of non-local correlations, whose evolution is consistent with a logarithmic growth of entanglement entropy, the hallmark of many-body localization. Our work experimentally establishes many-body localization as a qualitatively distinct phenomenon from localization in non-interacting, disordered systems.

2.1 Entanglement and quantum thermalization

Isolated quantum many-body systems, undergoing unitary time evolution, maintain their initial global purity. However, the presence of interactions drives local thermalization: the coupling between any subsystem and its remainder mimics the contact with a bath. This causes the

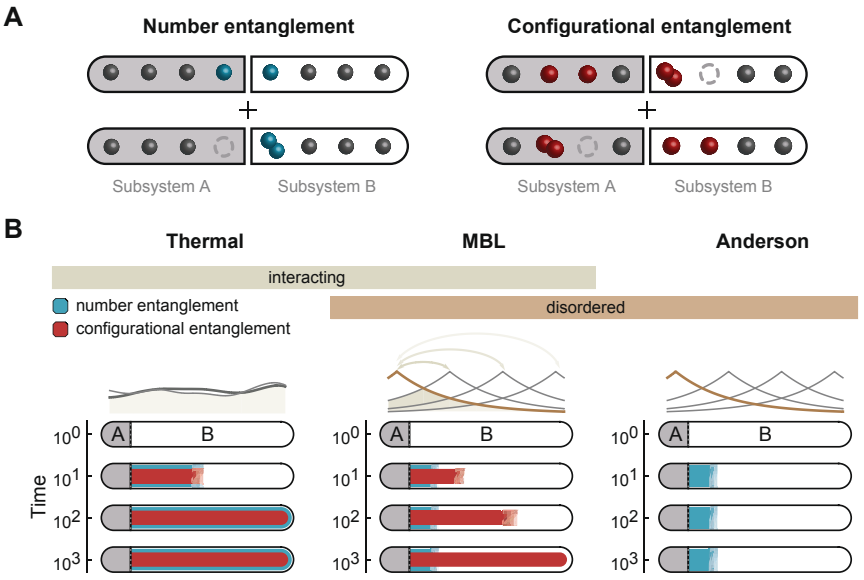

Fig. 1: Entanglement dynamics in non-equilibrium quantum systems. (A) *Subsystems A and B of an isolated system out of equilibrium entangle in two different ways: number entanglement stems from a superposition of states with different particle numbers in the subsystems and is generated through particle motion across the boundary; configurational entanglement stems from a superposition of states with different particle arrangement within the subsystems and requires both particle motion and interactions.* ***(B)*** *In the absence of disorder, both types of entanglement rapidly spreads across the entire system due to delocalization of particles (left panel). The degree of entanglement and the timescales change drastically when applying disorder (central panel): particle localization spatially restricts number entanglement, yet interactions allow configurational entanglement to form very slowly across the entire system. A disordered system without interactions shows only local number entanglement while the slow growth of configurational entanglement is completely absent (right panel).*

subsystem's degrees of freedom to be ultimately described by a thermal ensemble, even if the full system is in a pure state [4–6]. A consequence of thermalization is that local information about the initial state of the subsystem gets scrambled and transferred into non-local correlations that are only accessible through global observables [7–9].

Disordered systems [10–21] can provide an exception to this paradigm of quantum thermalization. In such systems, particles can localize and transport ceases, which prevents thermalization. This phenomenon is called many-body localization (MBL) [9, 10, 22–26]. Experimental studies have identified MBL through the persistence of the initial density distribution [27–32] and two-point correlation functions during transient dynamics [28]. However, while particle transport is frozen, the presence of interactions gives rise to slow coherent many-body dynamics that generate non-local correlations, which are inaccessible to local observables [33–35]. These dynamics are considered to be the hallmark of MBL and distinguish it from its non-interacting counterpart, called Anderson localization [10–14, 17, 18, 21]. Their observation, however, has remained elusive, because it requires exquisite control over the system's coherence.

We study these many-body dynamics by probing the entanglement properties of an MBL system with fixed particle number [33–37]. We distinguish two types of entanglement that can exist

between a subsystem and its complement (Fig. 1A): *Number entanglement* implies that the particle number in one subsystem is correlated with the particle number in the other. It is generated through tunneling across the boundary between the subsystems. *Configurational entanglement* implies that the configuration of the particles in one subsystem is correlated with the configuration of the particles in the other. It arises from a combination of particle motion and interaction. The formation of particle and configurational entanglement changes in the presence or absence of interactions and disorder in the system (Fig. 1B). In thermal systems without disorder, interacting particles delocalize and rapidly create both types of entanglement throughout the entire system. Contrarily, for Anderson localization, number entanglement builds up only locally at the boundary between the two subsystems. Here the lack of interactions prevents the substantial formation of configurational entanglement. In MBL systems, number entanglement builds up in a similarly local way as for Anderson localization. However, notably, the presence of interactions additionally enables the slow formation of configurational entanglement throughout the entire system.

In this work, we realize an MBL system and characterize these key properties: breakdown of quantum thermalization, finite localization length of the particles, area-law scaling of the number entanglement, and slow growth of the configurational entanglement that ultimately results in a volume-law scaling. Each property shows a contrasting behavior when the system is prepared at weak disorder in a thermalizing state. While the former three properties are also present for an Anderson localized state, the slowly growing configurational entanglement qualitatively distinguishes our system from a non-interacting, localized state.

2.2 Experimental system

In our experiments, we study MBL in the interacting Aubry-André model for bosons in one dimension [38, 39], which is described by the Hamiltonian

$$\hat{\mathcal{H}} = -J \sum_i \left(\hat{a}_i^\dagger \hat{a}_{i+1} + h.c.\right) + \frac{U}{2} \sum_i \hat{n}_i \left(\hat{n}_i - 1\right) + W \sum_i h_i \, \hat{n}_i \,, \tag{1}$$

where $\hat{a}_i^\dagger$ $\left(\hat{a}_i\right)$ is the creation (annihilation) operator for a boson on site i, and $\hat{n}_i = \hat{a}_i^\dagger \hat{a}_i$ is the particle number operator on that site. The first term describes the tunneling between neighboring lattice sites with the rate $J/\hbar$, where $\hbar$ is the reduced Planck constant. The second term represents the energy shift U when multiple particles occupy the same site. The last term introduces a site-resolved potential offset, which is created with an incommensurate lattice $h_i = \cos\left(2\pi\beta i + \phi\right)$ of period $\beta \approx 1.618$ lattice sites, phase ϕ, and amplitude W. In our experiment, we achieve independent control over J, W, and ϕ (Fig. 2A).

Our experiments begin with a Mott-insulating state in the atomic limit with one ^{87}Rb atom on each site of a two-dimensional optical lattice (Fig. 2B). The system is placed in the focus of a high-resolution imaging system through which we project site-resolved optical potentials [40]. We first isolate a single, one-dimensional chain from the Mott insulator and then add the site-resolved potential offsets W_i with the incommensurate lattice. At this point, the system

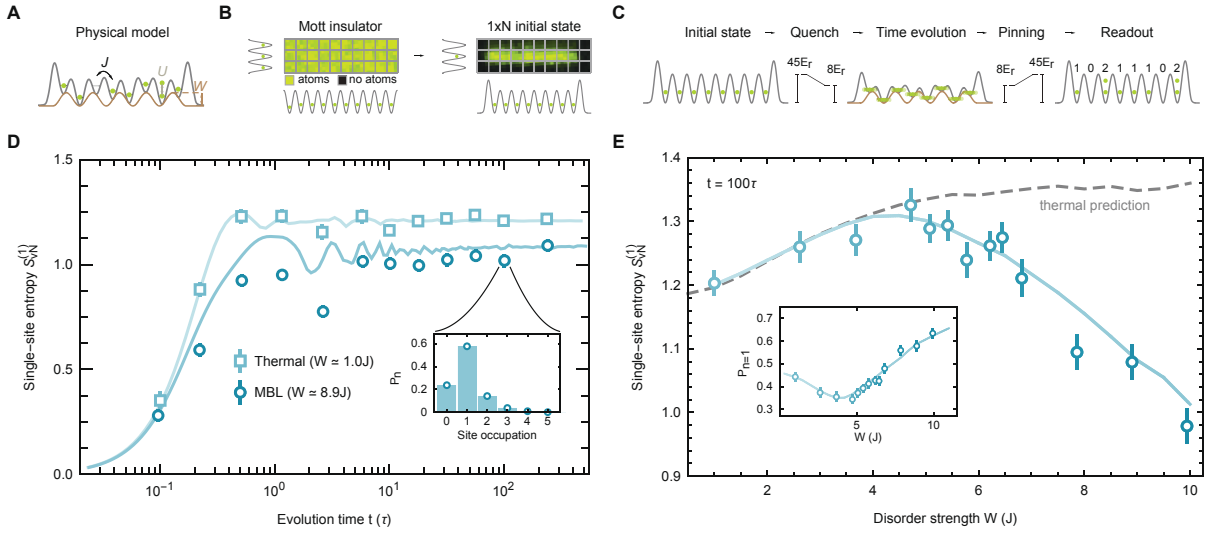

Fig. 2: Site-resolved measurement of thermalization breakdown. **(A)** *One dimensional Aubry-André model with particle tunneling at rate $J/\hbar$, on-site interaction energy U and quasi-periodic potential with amplitude W.* **(B)** *We prepare the initial state of eight unentangled atoms by projecting tailored optical potentials on a two-dimensional Mott insulator at $45E_r$ lattice depth, where $E_r = h\times 1.24\,kHz$ is the recoil energy.* **(C)** *We create a non-equilibrium system by abruptly enabling tunneling dynamics. Following a variable evolution time, we project the many-body state back onto the number basis by increasing the lattice depth, and obtain the site-resolved atom number from a fluorescence image).* **(D)** *We compute the single-site von Neumann entropy $S_{vN}^{(1)}$ from the site-resolved atom number statistics (inset) after different evolution times (scaled with tunneling time $\tau = \hbar/J$) in the presence of weak and strong disorder.* **(E)** *Probability p_1 to retrieve the initial state (inset) and $S_{vN}^{(1)}$ for different W, measured after 100τ evolution. The deviation from the thermal ensemble prediction for strong disorder signals the breakdown of thermalization in the system. All lines in* **(C-D)** *show the prediction of exact diagonalization calculations without any free parameters. Each data point is sampled from 197 disorder realizations).*

remains in a product state of one atom per lattice site. We abruptly switch on the tunneling by reducing the lattice depth within a fraction of the tunneling time (Fig. 2C). This quench brings the system to a non-equilibrium state and initializes the unitary time dynamics corresponding to the above Hamiltonian. The tunneling time $\tau = \hbar/J = 4.3(1)$ ms and the interaction strength $U = 2.87(3)J$ remain constant in all our experiments. Following a variable evolution time, we abruptly increase the lattice depth and image the system in an atom-number-sensitive way with single-site resolution). This projects the many-body state onto the number basis, which consists of all possible distributions of the particles within the chain.

In some realizations, particle loss during the time evolution and imperfect readout reduce the number of detected atoms compared to the initial state, thereby injecting classical entropy into the system. We eliminate this entropy by post-selecting the data on the intended atom number, thereby reaching a fidelity of $99.1(2)\%$ unity filling in the initial state, which is limited by the fraction of doublon-hole pairs in the Mott insulator. The result is a highly pure state, in which all correlations are expected to stem from entanglement in the system.

2.3 Breakdown of thermalization

We first investigate the breakdown of thermalization in a subsystem that consists of a single lattice site. The conserved total atom number enforces a one-to-one correspondence between the particle number outcome on a single site and the number in the remainder of the system—entangling the two during tunneling dynamics. Ignoring information about the remaining system puts the subsystem into a mixed state of different number states. The associated number entropy is given by $S_{\mathrm{n}}^{(1)} = -\sum_n p_n \log(p_n)$, where p_n is the probability of finding n atoms in the subsystem. Since the atom number is the only degree of freedom of a single lattice site, $S_{\mathrm{n}}^{(1)}$ captures all of the entanglement between the subsystem and its complement, and is equivalent to the single-site von Neumann entanglement entropy $S_{\mathrm{vN}}^{(1)}$.

Counting the atom number on an individual lattice site in different experimental realizations allows us to obtain the probabilities p_n and compute $S_{\mathrm{vN}}^{(1)}$. We perform such measurements for various evolution times. At low disorder depth $\big(W = 1.0(1)J\big)$, the entropy grows over a few tunneling times and then reaches a stationary value (Fig. 2D). The stationary value is reduced for deep disorder $\big(W = 8.9(1)J\big)$ and remains constant over two orders of magnitude, up to several hundred tunneling times. The lack of entropy increase indicates the absence of heating in the system. The excellent agreement of the measured entropy with *ab initio* calculations up to the longest measured evolution times suggests a highly unitary evolution of the system.

We perform measurements of $S_{\mathrm{vN}}^{(1)}$ at different disorder strengths following an evolution of one hundred tunneling times (Fig. 2E). To evaluate the degree of local thermalization, we compare the results with the prediction of a thermal ensemble for our system. For weak disorder, the measured entropy agrees with the predicted value, whereas the entropy is significantly reduced for strong disorder—signaling the absence of thermalization in the system. As a consequence, the system retains some memory of its initial conditions for arbitrarily long evolution times. We indeed find that the probability to retrieve the initial state of one atom per site increases for strong disorder (inset Fig. 2E).

2.4 Spatial localization

The breakdown of thermalization is expected to be a consequence of the spatial localization of the particles. Previous experiments have determined the decay length of an initially prepared density step into empty space [30]. We measure the localization by directly probing density-density correlations within the system. They are captured by $G^{(2)}(d) = \langle n_i n_{i+d}\rangle - \langle n_i\rangle\langle n_{i+d}\rangle$, where $\langle\cdots\rangle$ denotes averaging over different disorder realizations as well as all sites i of the chain. The particle numbers on two sites at distance $d > 0$ are uncorrelated for $G^{(2)}(d) = 0$. If a particle moves a distance d, the sites become anti-correlated, and the correlator decreases to $G^{(2)}(d) < 0$.

We measure the density-density correlations $G^2(d)$ for different disorder strengths in the stationary regime (Fig. 3A). For low disorder, we find the correlations to be independent of distance and below zero. This indicates that the particles tunnel across the entire system and hence are delocalized. On the other hand, at strong disorder, only nearby sites show significant correla-

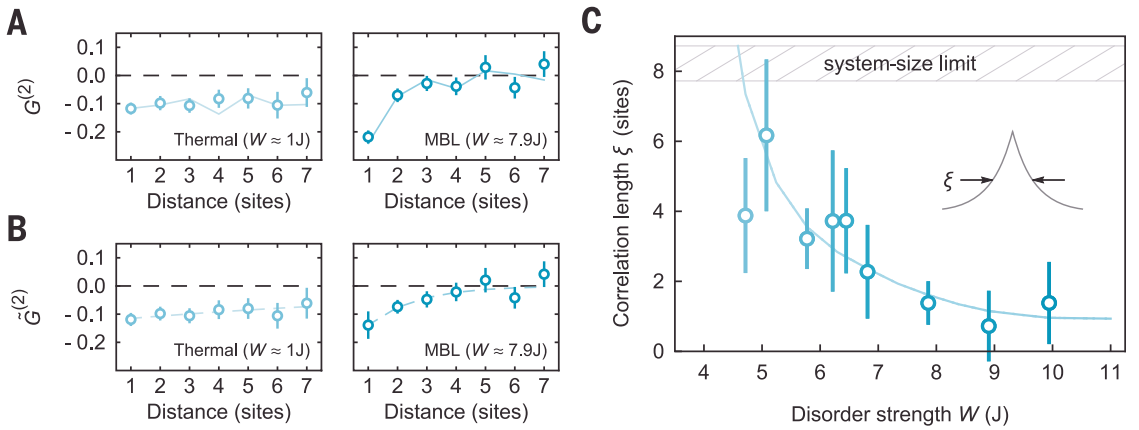

Fig. 3: Spatial localization of the particles. (A) *The density-density correlations* $G^{(2)}(d)$ *as a function of distance* d *at weak and strong disorder after an evolution time of* 100τ*. The alternating nature of the density-density correlations is imprinted by the autocorrelation function of the quasiperiodic potential.* **(B)** *Subtracting the influence of the quasiperiodic potential reveals the exponential decay of the correlation function.* **(C)** *Particle motion is confined within the correlation length* ξ*. We use a fit to extract* ξ *for different disorder strengths. The fit function is a product of an exponential decay with the autocorrelation function of the quasiperiodic potential. Each measurement is sampled from 197 disorder realizations. The solid lines show the prediction of exact diagonalization—calculated without any free parameters. Error bars denote the standard error of the mean in* **(A-B)***, and the fit error in* **(C)**.

tions, signaling the absence of particle motion across large distances. We thus conclude that the particles are localized. We extract the correlation length by fitting an exponentially decaying function to the data (Fig. 3B). For increasing disorder, the correlation length decreases from the entire system size down to around one lattice site (Fig. 3C).

Our observation of localized particles is consistent with the description of MBL in terms of local integrals of motion [33–35]. It describes the global eigenstates as product states of exponentially localized orbitals. The correlation length extracted from our data is a measure of the size of these orbitals. Since the latter form a complete set of locally conserved quantities, this picture connects the breakdown of thermalization in MBL with non-thermalizing, integrable systems.

2.5 Dynamics and spreading of entanglement

We now turn to a characterization of the entanglement properties of larger subsystems, starting with a subsystem covering half the system size. As for the case of a single lattice site, the particle number in the subsystem can become entangled with the number in the remaining system through tunneling dynamics, resulting in the number entropy $S_{\mathrm{n}} = -\sum_n p_n \log(p_n)$. However, subsystems which extend over several lattice sites, with a given particle number, offer the particle configuration as an additional degree of freedom for the entanglement. Configurational entanglement only builds up substantially in interacting systems, since configurational correlations require several particles. The associated configurational entropy S_{c}, together with the number entropy, forms the von Neumann entropy, $S_{\mathrm{vN}} = S_{\mathrm{n}} + S_{\mathrm{c}}$. An analogous relation exists for spin systems with conserved total magnetization instead of the particle number.

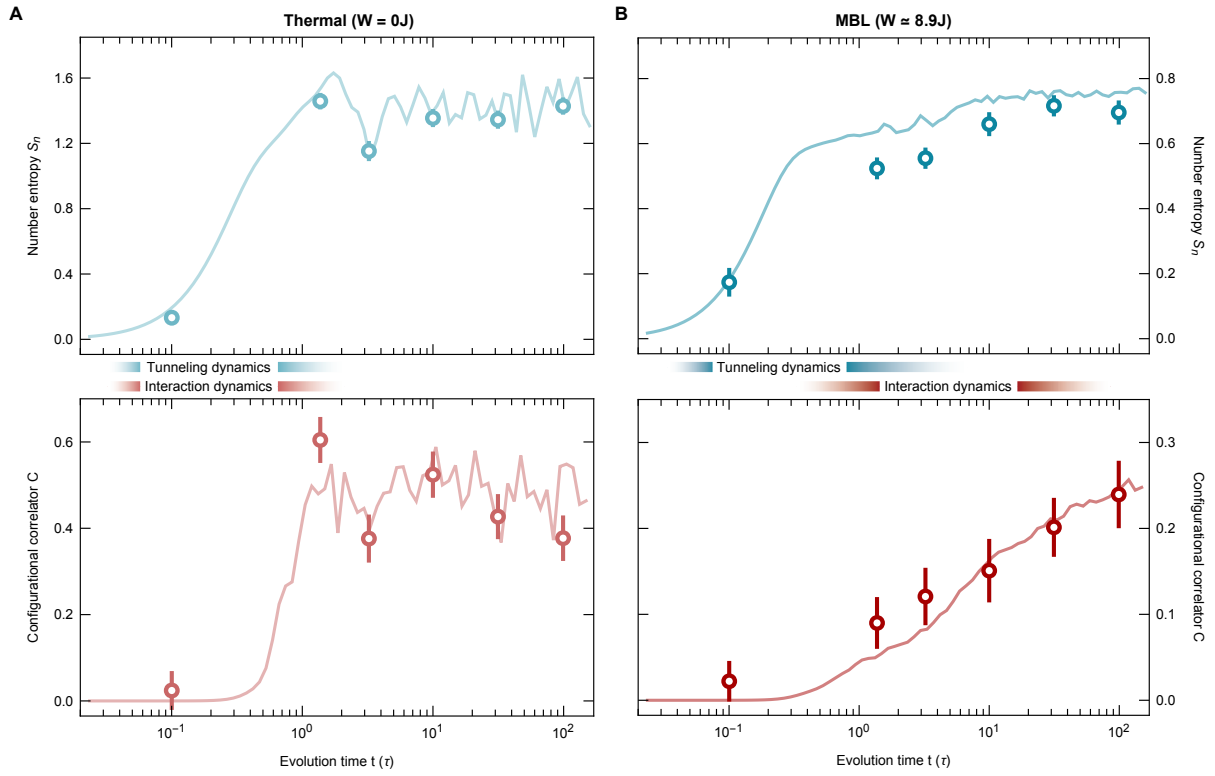

Fig. 4: Dynamics of number and configurational entanglement. **(A)** *In the thermal regime, both the number entropy S_n and the configurational correlator C quickly rise and reach a stationary value after thermalization.* **(B)** *We observe different time scales in the MBL regime. S_n increases for a longer time and reaches a stationary value that is suppressed compared to the thermal one. C shows a persistent slow increase that is consistent with a logarithmic growth, until the longest evolution times covered by our measurements. The solid lines show the prediction of exact diagonalization calculations without any free parameters. The above data was taken on a six-site system and averaged over four disorder realizations.*

The dynamics of S_n and S_c in the MBL regime (Fig. 4A) can be understood in the picture of localized orbitals. Since the localized orbitals restrict the particle motion, the number entropy can only develop within the localization length and hence S_n saturates at a lower value than for the thermal case. In the MBL regime, disorder suppresses the tunneling. Therefore, saturation is reached at a later time. However, the dynamics of S_c are strikingly different. The bare on-site interaction and particle tunneling combine into an effective interaction among localized orbitals, which decays exponentially with the distance between them. As a consequence, entanglement between distant orbitals forms slowly, causing a logarithmic growth of S_c, even after S_n has saturated [33–37].

In our experiment, we can independently probe both types of entanglement. We obtain the number entropy S_n through the probabilities p_n by counting the atom number in the subsystem in different experimental realizations. The configurational entropy S_c, in contrast, is challenging to measure in a many-body system since it requires experimental access to the coherences between a large number of quantum states [41,42]. Here we choose a complementary approach

to probe the configurational entanglement in the system. It exploits the configurational correlations between the subsystems, quantified by the correlator

$$C = \sum_{n=0}^{N} p_n \sum_{\{A_n\},\{B_n\}} \left| p(A_n \otimes B_n) - p(A_n)\, p(B_n) \right|, \tag{2}$$

where $\{A_n\}$ (and $\{B_n\}$) is the set of all possible configurations of n particles in subsystem A (and $N-n$ in B), where N is total number of particles in the system. All probability distributions are normalized within the subspaces of n particles in A and the remaining $N-n$ particles in B. The configuration $A_n \otimes B_n$ is separable if $p(A_n \otimes B_n) = p(A_n)\, p(B_n)$. The correlator therefore probes the entanglement through the deviation from separability between A and B. In the MBL regime, for sufficiently small amounts of entanglement, we numerically find C to be proportional to S_{c}, and hence it inherits its scaling properties. This criterion is independent of the system size. Our measurements lie within the numerically verified parameter regime.

We study the time dynamics of S_{n} and C with and without disorder (Fig. 4B, C). Without disorder, both S_{n} and C rapidly rise and reach a stationary value within a few tunneling times (insets). In the presence of strong disorder, we find a qualitatively different behavior for the two quantities: S_{n} reaches a stationary state within few tunneling times, although after longer evolution time due to reduced effective tunneling. Additionally the stationary value is significantly reduced, indicating suppressed particle transport through the system. The correlator C, in contrast, shows a persistent slow growth up to the longest evolution times reached by our measurements. The growth is consistent with logarithmic behavior over two decades of time evolution. We conclude that we observe interaction-induced dynamics in the MBL regime, which are consistent with the phenomenological model [33–35]. The agreement of the long-term dynamics of S_{p} and C with the numerical calculations in the MBL regime confirms the unitary evolution of the system over $100\,\tau$. The system remains in the finite-time limit, not in the finite-size limit, since the spread of entanglement has not yet stopped at the longest studied evolution times.

Considering the entropy in subsystems of different size gives us insights into the spatial distribution of entanglement in the system: in a one-dimensional system, locally generated entanglement results in a subsystem size independent entropy, whereas entanglement from non-local correlations causes the entropy to increase in proportion to the size of the subsystem. In reference to the subsystem's boundary and volume, these scalings are called area law and volume law. We find almost no change in S_{n} for different subsystems of an MBL system (Fig. 5A), indicating an area law scaling due to localized particles and confirming that particle transport is suppressed. In contrast, the configurational correlations C increase until the subsystem reaches half the system size (Fig. 5B). Such a volume-law scaling is also expected for the entanglement entropy and demonstrates that the observed logarithmic growth indeed stems from non-local correlations across the entire system.

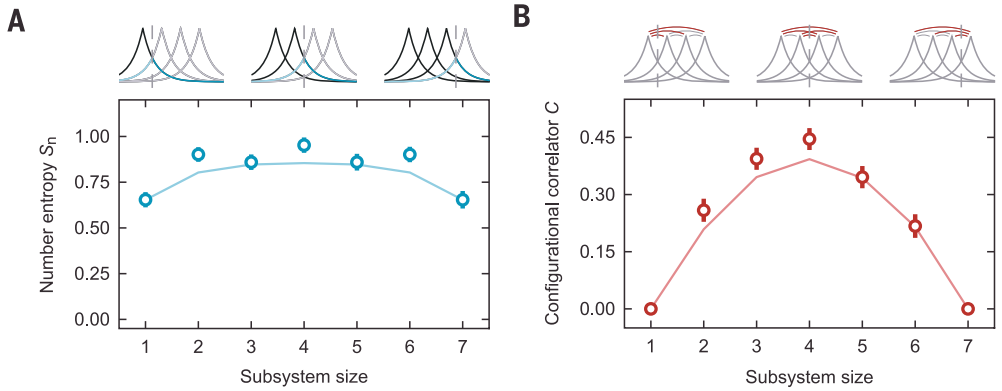

Fig. 5: Spatial distribution of the entanglement. *Number entropy and configurational correlator in the MBL regime ($W = 8.9\,J$) after an evolution time of 100τ.* **(A)** *In an MBL system, number fluctuations between two subsystems only stem from local orbitals near the boundary. Consequentially, the number entropy S_n does not depend on the subsystem size, i.e., follows an area law..* **(B)** *After long evolution times, each local orbital is configurationally entangled with every other. Hence, the configurational correlator C increases almost linearly with the subsystem size, showing a volume-law behavior. The solid lines show the prediction of exact diagonalization calculations without any free parameters. The above data was averaged over four disorder realizations.*

2.6 Conclusion

Investigating the growth of non-local quantum correlations has been a long-standing experimental challenge for the study of MBL systems. In addition to achieving exceptional isolation from the environment and local access to the system, such a measurement requires access to the entanglement entropy [41]. Our work provides a novel method to characterize the entanglement properties of MBL systems. Since it is based on measurements of the particle number fluctuations and their configurations, the method is experimentally accessible and can be generalized to higher dimensions and different experimental platforms, where a direct measurement of entanglement entropy remains challenging, e.g., trapped ions, neutral atoms, and superconducting circuits. The observation of slow coherent many-body dynamics along with the breakdown of thermalization coincides with the expected behavior for larger systems, and allows us to unambiguously identify and characterize the MBL state in our system.

The eight-site system constrained to unity filling, which is studied in this work, spans a 6435-dimensional Hilbert space—larger than for a system of 14 spin-1/2 particles constrained to zero total magnetization. In the future, experiments at even larger system sizes will be of interest to shed light on the critical properties of the thermal-to-MBL phase transition, which are the subject of ongoing studies [43–46]. In our system, it is experimentally feasible to increase the system size at unity filling to a numerically intractable regime. Additionally, we have full control over the disorder potential on every site, which opens the way to studying the role of rare regions and Griffiths dynamics as well as the long-time behavior of an MBL state with a link to a thermal bath [47–49]. Ultimately, these studies will further our understanding of quantum thermodynamics and whether such systems are suitable for future applications as quantum memories [9].

3 Critical behavior

Phase transitions are driven by collective fluctuations of a system's constituents that emerge at a critical point [50]. This mechanism has been extensively explored for classical and quantum systems in equilibrium, whose critical behavior is described by a general theory of phase transitions. Recently, however, fundamentally distinct phase transitions have been discovered for out-of-equilibrium quantum systems, which can exhibit critical behavior that defies this description and is not well understood [50]. A paradigmatic example is the many-body-localization (MBL) transition, which marks the breakdown of quantum thermalization [23, 51, 34, 35, 52, 26–28, 30, 53]. Characterizing quantum critical behavior in an MBL system requires probing its entanglement properties over space and time [34, 35, 26], which has proven experimentally challenging due to stringent requirements on quantum state preparation and system isolation. Here, we observe quantum critical behavior at the MBL transition in a disordered Bose-Hubbard system and characterize its entanglement properties via its quantum correlations. We observe strong correlations, whose emergence is accompanied by the onset of anomalous diffusive transport throughout the system, and verify their critical nature by measuring their system-size dependence. The correlations extend to high orders in the quantum critical regime and appear to form via a sparse network of many-body resonances that spans the entire system [44, 45]. Our results connect the macroscopic phenomenology of the transition to the system's microscopic structure of quantum correlations, and they provide an essential step towards understanding criticality and universality in non-equilibrium systems [50, 45, 26].

3.1 The many-body localization transition

The many-body-localization (MBL) transition describes the breakdown of thermalization in an isolated quantum many-body system as disorder is increased beyond a critical value [27, 28, 30, 53]. It represents a novel type of quantum phase transition that fundamentally differs from both its classical and quantum ground-state counterparts [23, 51, 26]. Instead of being characterized by an instantaneous thermodynamic signature, it is identified by the system's inherent dynamic behavior. In particular, the MBL transition manifests itself through a change in entanglement dynamics [26, 53]. Recent years have seen tremendous progress in our understanding of both the thermal and the MBL phases within the frameworks of quantum thermalization [52, 7, 8] and emergent integrability [34, 35, 27, 28, 30, 53], respectively.

The quantum critical behavior at this transition, however, has remained largely unresolved [26]. In particular, it is unclear whether the traditional association of collective fluctuations with static and dynamic critical behavior can be applied to this transition. The high amount of entanglement found at the MBL transition limits numerical studies due to the required computational power [54, 55]. Several theoretical approaches, despite using disparate microscopic structures, suggest anomalous transport as the macroscopic behavior at the quantum critical point [43, 44, 56, 57]. Experimental studies indeed indicate a slowdown of the dynamics at intermediate disorder [46, 58]. However, identifying anomalous transport as quantum criti-

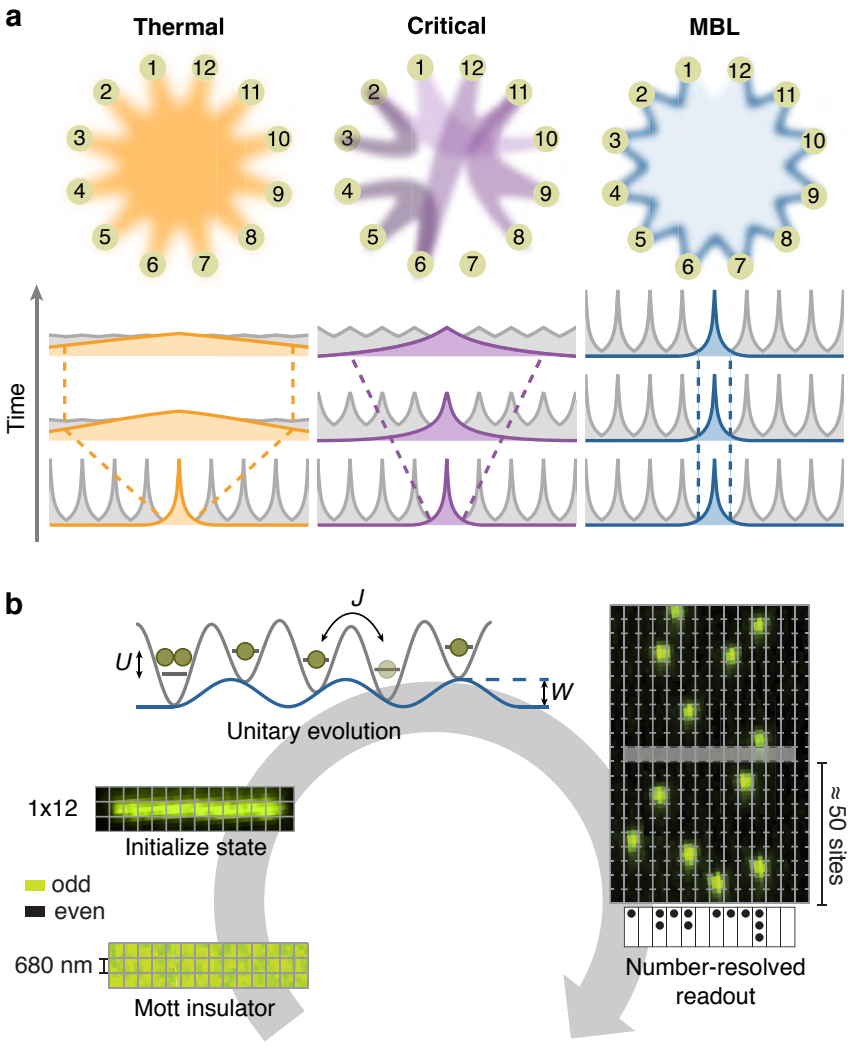

Fig. 6: ***Microscopy of the many-body localization transition. a:*** *The quantum state at the critical point takes on a complex pattern of strong multi-particle correlations at all length scales, visualized by shaded links between different lattice sites. In contrast, it simplifies in the thermal and the MBL phases to maximal entanglement and predominantly local correlations, respectively. A consequence is a change in the transport properties from diffusive to anomalous before ceasing completely in MBL.* ***b:*** *We initialize the system as a pure product state of up to twelve lattice sites at unity filling. The system becomes entangled under the unitary, non-equilibrium dynamics of the bosonic, interacting Aubry-André model with on-site interaction energy U, particle tunneling at rate $J/\hbar$ (with the reduced Planck constant $\hbar$), and quasi-periodic potential with amplitude W. After a variable evolution time, we obtain the full atom-number distribution from site-resolved fluorescence imaging after expansion.*

cal dynamics is experimentally challenging, since similar behavior can also originate from stochastic effects such as inhomogeneities in the initial state [59], or the coupling to a classical bath [60, 31]. Additionally, in the case of random disorder, the presence of rare-regions admits several microscopic mechanisms that may govern this critical behavior and therefore makes identifying this mechanism challenging [47–49]. Our experimental protocol overcomes these challenges by using a quasi-periodic potential, which is rare-region free, as well as by

evolving a pure, homogeneous initial state under unitary dynamics. Using this protocol, we observe quantum critical dynamics via anomalous transport, enhanced quantum fluctuations, and system-size dependent thermalization. In addition, we microscopically resolve and characterize the structure of the entanglement in the many-body states through their multi-particle quantum correlations.

Our experiments start with a pure state of up to twelve unentangled lattice sites at unity filling. We study its out-of-equilibrium evolution after a rapid increase of the tunneling in the bosonic, interacting Aubry-Andre Hamiltonian

$$\hat{\mathcal{H}} = -J \sum_i \left(\hat{a}_i^\dagger \hat{a}_{i+1} + h.c.\right) + \frac{U}{2} \sum_i \hat{n}_i \left(\hat{n}_i - 1\right) + W \sum_i h_i \hat{n}_i \,,$$

where $\hat{a}_i^\dagger$ $\left(\hat{a}_i\right)$ is the creation (annihilation) operator for a boson on site i, and $\hat{n}_i$ is the corresponding particle number operator. The tunneling time $\tau = \hbar/J = 4.3(1)$ ms (with the reduced Planck constant $\hbar$) between neighboring sites and the pair-wise interaction energy $U = 2.87(3)J$ remain constant for all experiments. The potential energy offset $h_i = \cos\left(2\pi\beta i + \phi\right)$ on site i follows a quasi-periodic distribution of amplitude W, period $1/\beta \approx 1.618$ lattice sites, and phase ϕ. After a variable evolution time, we obtain full counting statistics of the quantum state through a fluorescence imaging technique. The applied unitary evolution preserves the initial purity of $99.1(2)\%$ per site, such that all correlations are expected to stem from entanglement in the system [8, 53].

3.2 Transport properties

We first characterize the system's dynamical behavior by studying its transport properties for different disorder strengths. Since the initial state has exactly one atom per site, the system starts with zero density correlations at all length scales. However, during the Hamiltonian evolution, tunneling dynamics build up anti-correlated density fluctuations between coupled sites of increasing distance (Fig. 7a). Motivated by this picture, we quantify the particle dynamics by defining the transport distance, $\Delta x \propto \sum_d d \left\langle G_{\mathrm{c}}^{(2)}(i, i{+}d)\right\rangle_i$, as the first moment of the disorder-averaged two-point density correlations, $G_{\mathrm{c}}^{(2)}(i, i{+}d) = \langle \hat{n}_i \hat{n}_{i+d}\rangle - \langle \hat{n}_i\rangle\langle \hat{n}_{i+d}\rangle$ (Fig. 7a). At low disorder, we observe these anti-correlations rapidly build up and saturate over a time scale of $t/\tau \approx L/2$. With increasing disorder, we observe a slowdown of particle transport that is consistent with a power-law growth $\Delta x \sim t^\alpha$ (Fig. 7b) [61]. We extract the anomalous diffusion exponent α from a subset of the data points that exclude the initial transient dynamics in the system ($L/2 < t/\tau \leq 100$) (Fig. 7b inset). The exponent α is reduced by successively higher disorder, demonstrating the suppression of transport in the MBL regime.

In order to identify the anomalous diffusion as a signature of quantum critical dynamics, we measure the system-size dependence of two observables in the long-time limit ($t = 100\tau$): the on-site number fluctuations $\mathcal{F} \equiv G_{\mathrm{c}}^{(2)}(d{=}0)$ as a probe of local thermalization, and the transport distance Δx as a localization measure (Fig. 7c). At low disorder, the fluctuations agree with those predicted by a thermal ensemble and particles are completely delocalized for both system

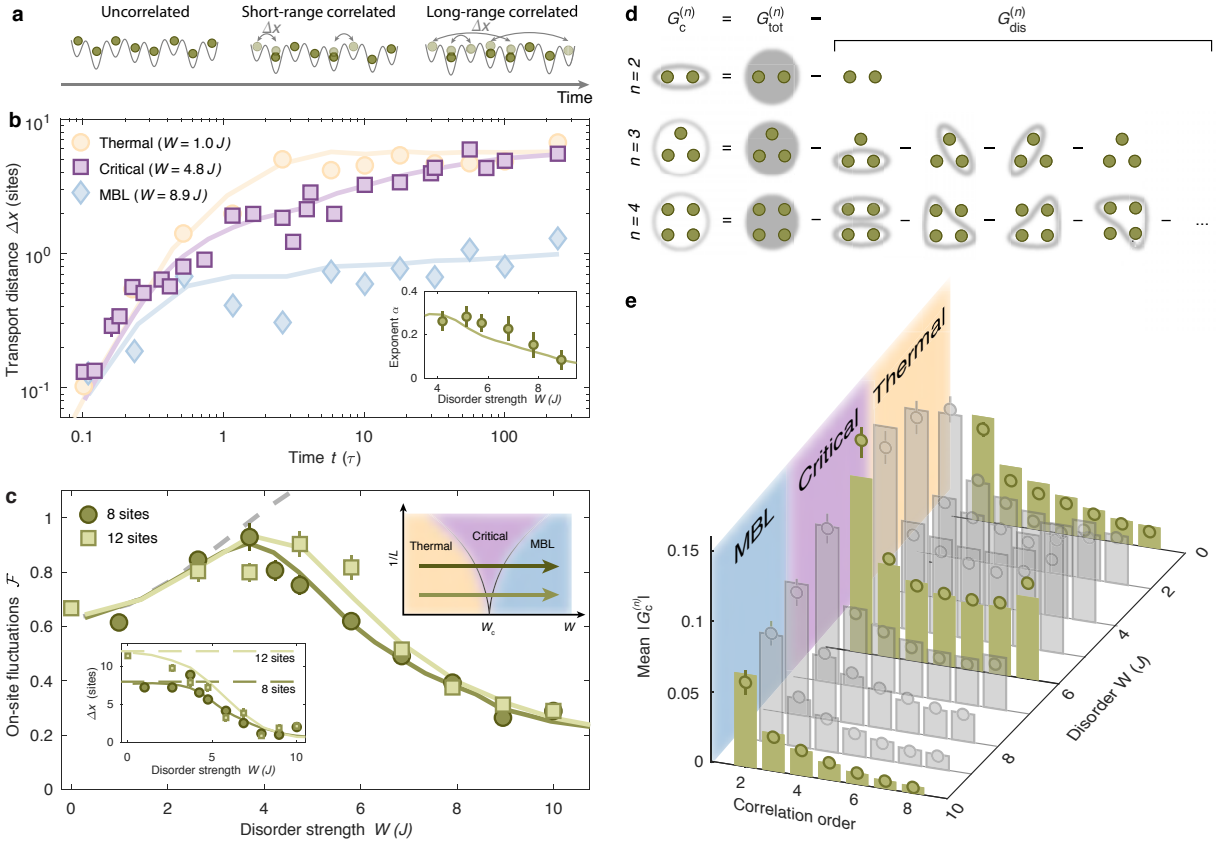

Fig. 7: ***Quantum critical dynamics at the MBL transition.*** ***a:*** *The initially uncorrelated system develops two-point density correlations under its transport dynamics. Short-range correlations emerge within one tunneling time $\tau{=}\hbar/J$, whereas the diffusion exponent α determines the time scale over which correlations form across the system size L.* ***b:*** *Particle transport slows down at intermediate disorder, consistent with a power-law evolution with exponent $\alpha{<}0.5$, demonstrating subdiffusive dynamics (inset). These data were taken on an eight-site system.* ***c:*** *The critical nature of these dynamics is determined from the behavior of on-site density fluctuations $\mathcal{F}$ and transport distance $\Delta\tilde{x}$ (lower left inset) for both considered system sizes. The thermal regime is determined by the agreement of the measured $\mathcal{F}$ with the prediction from a thermal ensemble (dashed grey). The system-size dependence at intermediate disorder is consistent with the reduced size of a quantum critical cone (upper right inset). These data were measured for both an eight-site and twelve-site system.* ***d:*** *We obtain the genuine many-body processes of order n from connected correlations $G_c^{(n)}$ by subtracting all lower order contributions $G_{dis}^{(n)}$ from the total correlation function $G_{tot}^{(n)}$.* ***e:*** *In the quantum critical regime, we find enhanced collective fluctuations at all measured orders by computing the mean absolute value of $G_c^{(n)}$ for different disorder strengths. These data were measured on a twelve-site system. The solid lines (**b,c**) and bars (**e**) denote the prediction of exact numeric time calculations without any free parameters. The errorbars are the standard error of the mean and are below the marker size in **b**.*

sizes. This demonstrates that local quantum thermalization occurs independently of system size at low disorder and establishes that this regime corresponds to the system being in the thermal phase. At strong disorder, the physics is governed by the formation of an intrinsic length scale, namely the localization length $\xi \sim \Delta\tilde{x}$ [30, 53]. We observe system-size independent, sub-

thermal fluctuations and measure an intrinsic length scale $\Delta\tilde{x}$. This indicates that the strong disorder regime corresponds to the system being in the localized phase. However, at intermediate disorder, we find a system-size dependence for both observables. This demonstrates the absence of an intrinsic length scale and the presence of finite-size-limited fluctuations, identifying that the system is in a critically thermalizing regime. These measurements of system-size-dependent thermalization can be visualized as two horizontal cuts in a finite-size phase diagram. The observed finite-size dependence is consistent with the physics associated with a critically thermalizing intermediate phase and a shrinking quantum critical cone (Fig. 7c inset) [50].

3.3 Multi-particle correlations

We then investigate the multi-particle correlations in the system to probe the presence of enhanced quantum fluctuations in the quantum critical regime (Fig. 7d). For this study, we employ the n-point connected density-correlation functions [62–64],

$$G_{\mathrm{c}}^{(n)}(\mathbf{x}) = G_{\mathrm{tot}}^{(n)}(\mathbf{x}) - G_{\mathrm{dis}}^{(n)}(\mathbf{x}),$$

which act on lattice sites with positions $\mathbf{x} = (x_1, \ldots, x_n)$. The disconnected part of this function, $G_{\mathrm{dis}}^{(n)}$, is fully determined by all lower-order correlation functions, and therefore does not contain new information at order n. By removing it from the total measured correlation function, $G_{\mathrm{tot}}^{(n)}(\mathbf{x}) = \left\langle \prod_{k=1}^{n} \hat{n}(x_k) \right\rangle$, we isolate all n-order correlations that are independent of lower-order processes. This approach gives a direct handle on the level of complexity of the underlying many-body wave function and characterizes its entanglement via its non-separability into subsystems of size $< n$. We quantify the relevance of order n processes by computing the mean absolute value of all correlations arising from both contiguous and non-contiguous n sites in the system (Fig. 7e). We find that in the thermal and the many-body-localized regimes, the system becomes successively less correlated at higher order. The behavior in the quantum critical regime is strikingly different: we observe that the system is strongly correlated at all measured orders.

3.4 Site-resolved correlations

In order to reveal the microscopic origin for the anomalous transport, we now investigate the site-resolved structure of the many-body state (Fig. 8a). We first study how much each lattice site contributes to the transport by considering the site-resolved two-point correlations in the long-time limit ($t = 100\tau$). In the thermal regime, we find similar correlations between all lattice sites, which correspond to uniformly delocalized atoms. In contrast, density correlations are restricted to nearby sites in the MBL regime due to localization. Intriguingly, we observe a sparse structure of correlations at intermediate disorder, which involves only specific distances between lattice sites, yet spans the entire system size.

The sparse structure is expected to be linked to the applied quasi-periodic potential. The average energy offsets of sites d apart in the system are correlated by this potential. This correlation is

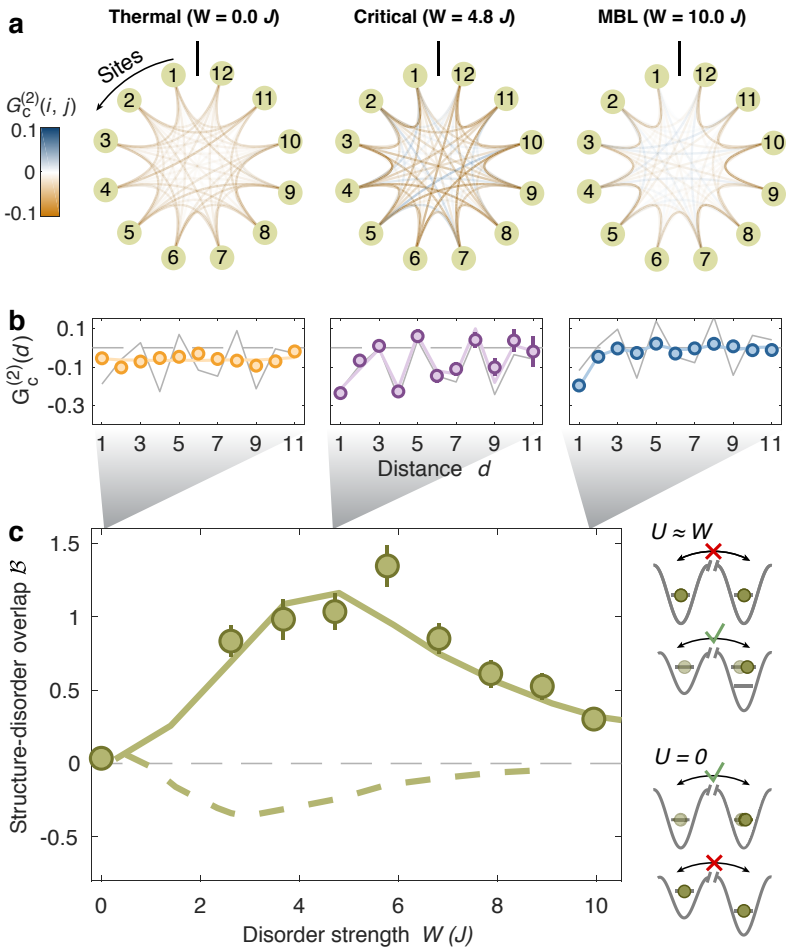

Fig. 8: ***Sparse network of resonances.*** ***a:*** *The measured site-dependent two-point correlations $G_c^{(2)}(i,j)$ are plotted for all inter-site combinations, whose amplitudes are represented by the colored lines connecting the lattice sites-i,j. In the quantum critical regime, correlations preferably form at specific distances, showing a network-like structure. This contrasts with homogeneous correlations in the thermal regime and nearest-neighbor correlations in the MBL regime.* ***b:*** *The structure of the correlation network is revealed by the averaged correlation function $G_c^{(2)}(d) = \left\langle G_c^{(2)}(i,i+d)\right\rangle_i$. Its similarity to the autocorrelation $A(d) = \langle h_i h_{i+d}\rangle_i$ of the quasi-periodic potential (solid grey) indicates interaction-induced tunneling processes that are enhanced when the interaction energy compensates for the potential energy difference.* ***c:*** *We quantify the similarity by the overlap $\mathcal{B} = \Sigma_d G_c^{(2)}(d)A(d)$, which is maximal in the quantum critical regime. The sign of the overlap would be opposite for non-interacting particles (dashed line), which favors tunneling between sites with similar potential energies. The solid lines in* ***b,c*** *and the dashed line in* ***c*** *denote the prediction of exact numeric time evolution calculations without any free parameters.*

then inherited by the system's fluctuations when the interaction energy U compensates for these correlated offsets. To investigate this structure, we compare the two-point density correlations with the autocorrelation function, $A(d) = \langle h_i h_{i+d}\rangle_i$, of the quasi-periodic potential. Indeed, we find that the site-averaged density correlations $G_c^{(2)}(d) = \langle G^{(2)}(i,i+d)\rangle_i$ inherit their spatial structure from $A(d)$ (Fig. 8b). We find that this contribution is maximal in the critical regime but

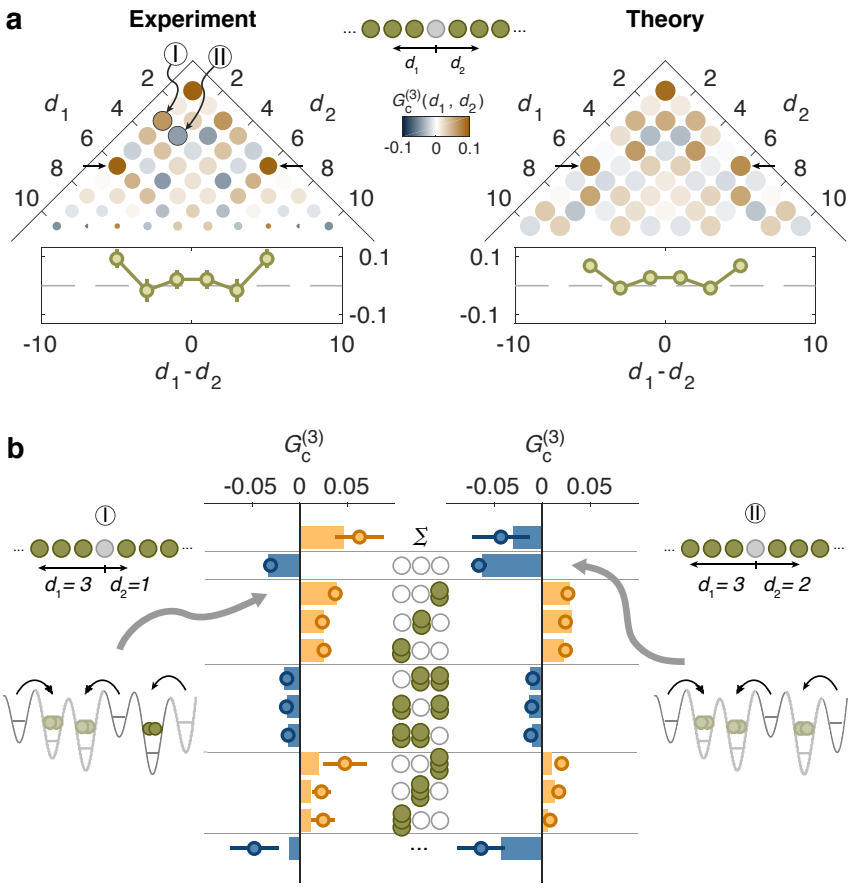

Fig. 9: ***Many-body correlations in the quantum critical regime. a:*** *The connected correlation function, $G_c^{(3)}(d_1, d_2)$, for three lattice sites spaced by distances d_1 and d_2 in the quantum critical regime ($W = 4.8J$), showing the strongly interacting nature of the state. We find that the three-point correlations show a characteristic structure that is governed by the contribution of the number states on the considered sites. The arrows indicate the cut in d_1, d_2 space plotted below.* ***b:*** *To exemplify the relevant processes of order $n = 3$, we show the contributions of the number states on lattice sites at distance $d_1 = 3$, $d_2 = 1$ (left) and $d_1 = 3$, $d_2 = 2$ (right). While there is a wide distribution of contributing configurations, the relative dominance of a particular process provides the overall structure in* ***a****. The illustration of atoms undergoing a highly correlated hopping process in the lattice describe how such correlations can contribute to either positive or negative correlations among the three considered sites. The theory plot in* ***a*** *and bars in* ***b*** *are calculated from exact numeric time calculations without any free parameters. The inverse marker size in the experimental plot in* ***a****, and the error bars in both* ***a*** *and* ***b*** *denote the standard error of the mean.*

is strongly reduced in the thermal and MBL regimes (Fig. 8c). These observations contrast with the behavior of a non-interacting system, where the sign of the structure is opposite since resonant tunneling is favored for zero potential energy difference (Fig. 8c). These results illustrate microscopically how the interplay of strong interactions and disorder can lead to anomalous diffusion. However, this picture of effective single-particle hopping that couples distant sites neglects the many-body nature of these systems.

3.5 Site-resolved detection of three-body processes

In order to investigate the system's many-body structure, we examine the site-resolved contributions of the three-point correlations. Since all non-zero contributions to the three-point correlations involve correlated hopping of at least two particles, they are a signature for multi-particle entanglement [63]. In the quantum critical regime, we find that these correlations span the entire system and are highly structured, taking on both positive and negative values (Fig. 9a). In contrast to the pattern in the second-order correlation function, this third-order structure is not directly recognizable as the quasi-periodic-potential correlations. In order to gain further insight into the structure, we analyze the contributions of all possible particle configurations in Fig. 9b. In particular, for $G_c^{(3)}(d_1{=}3, d_2{=}1)$, which is positive, we see that the dominant contribution comes from a particular process that favors multiple atoms hopping to the same site. In contrast, $G_c^{(3)}(d_1{=}3, d_2{=}2)$, which is negative, has a dominant process that favors all atoms leaving the three sites considered. While this provides some intuition for the emergent many-body resonances, the three-point correlations are, in fact, the result of a superposition of many correlated processes. These observations further demonstrate how the interactions between multiple atoms can compensate for the disorder via correlated tunneling of several atoms. In this way, we can see the additional role interactions play in the disordered system: they supply higher-order many-body resonances that preserve transport where lower-order processes are energetically suppressed.

3.6 Discussion and outlook

Our results demonstrate how a many-body, sparse resonant structure drives the quantum critical behavior at the MBL transition. This observed microscopic description is consistent with the theoretically suggested mechanisms of a sparse *backbone* of resonances that can act as a functional bath for the system [65, 44, 45]. However, our results provide a new perspective on this description by mapping out the prevalence of high-order processes in the system that facilitate this critical thermalization.

In future experiments, the tunability of our system will allow us to address further open questions on the MBL transition, such as possible discontinuities of the entanglement entropy [45], the potential emergence of new dynamic phases near the critical point, and the influence of rare-regions in the disorder potential [48, 49]. Furthermore, the demonstrated techniques pave the way to explore the role of universality in non-equilibrium systems. From a computational perspective, our system's Hilbert space dimension is comparable to the dimension of 22 spins with zero total magnetization. A moderate increase of the system's spatial dimension beyond this experiment results in numerically intractable sizes.

4 Quantum avalanches

Strongly correlated systems can exhibit unexpected phenomena when brought in a state far from equilibrium. An example is many-body localization, which prevents generic interacting

systems from reaching thermal equilibrium even at long times [66, 67]. The stability of the many-body localized phase has been predicted to be hindered by the presence of small thermal inclusions that act as a bath, leading to the delocalization of the entire system through an avalanche propagation mechanism [48, 49, 68–71]. Here we study the dynamics of a thermal inclusion of variable size when it is coupled to a many-body localized system. We find evidence for accelerated transport of the thermal inclusion into the localized region. We monitor how the avalanche spreads through the localized system and thermalizes it site by site by measuring the site-resolved entropy over time. Furthermore, we isolate the strongly correlated bath-induced dynamics with multipoint correlations between the bath and the system. Our results have implications on the robustness of many-body localized systems and their critical behavior.

4.1 Stability of many-body localized systems

One of the founding principles of statistical physics is that a generic macroscopic system can equilibrate on its own. This means that local fluctuations of energy, magnetization, or particle density can relax towards thermal equilibrium because interactions allow different parts of the system to serve as reservoirs to each other. This universal picture has been challenged by the idea of many-body localization (MBL), which suggests that systems with strong disorder can evade thermalization even in the presence of interactions [66, 67, 72, 73, 27, 30, 46, 1, 2]. In one-dimensional systems, a stable MBL phase can be argued for as follows: the matrix elements of local operators decay exponentially with the separation between two points, whereas the density of states increases exponentially with the system size. For strong disorder, matrix elements can thus be argued to decay faster than the density of states increases, ultimately inhibiting relaxation.

However, the existence of MBL remains a subject of debate, since it is unclear when those conditions are fulfilled [74–82]. For instance, by introducing a small region with weak disorder, part of the system may be delocalized and thus give rise to local operators with non-exponential decay [54, 83–89, 43–45, 47]. Those local weakly disordered regions occur naturally in randomly disordered systems, when potential offsets on consecutive lattice sites accidentally coincide [90, 91, 54, 85, 47]. The dynamics in MBL systems in the presence of a thermal region have been predicted to occur in so-called quantum avalanches, which imply that these regions grow by absorbing nearby disordered regions [48, 49, 68–70]. Under which conditions quantum avalanches can arise, run out of steam, or propagate without halt determines the fate of MBL at long evolution times. Their understanding is thus closely connected to discerning thermalization in interacting many-body systems.

4.2 Quantum avalanches

Perturbative bath-induced relaxation can often be captured in the context of Fermi's golden rule (Fig. 10a, left). In this picture, the relaxation rate $\Gamma_i = g_i^2 \rho_{\text{bath}}$ at a distance of i sites away from the bath is given by the product of the bath's constant density of states ρ_{bath} and the coupling rate $g_i \propto J e^{-i/\xi_{\text{loc}}}$, where ξ_{loc} is the localization length of the MBL system, and J is the

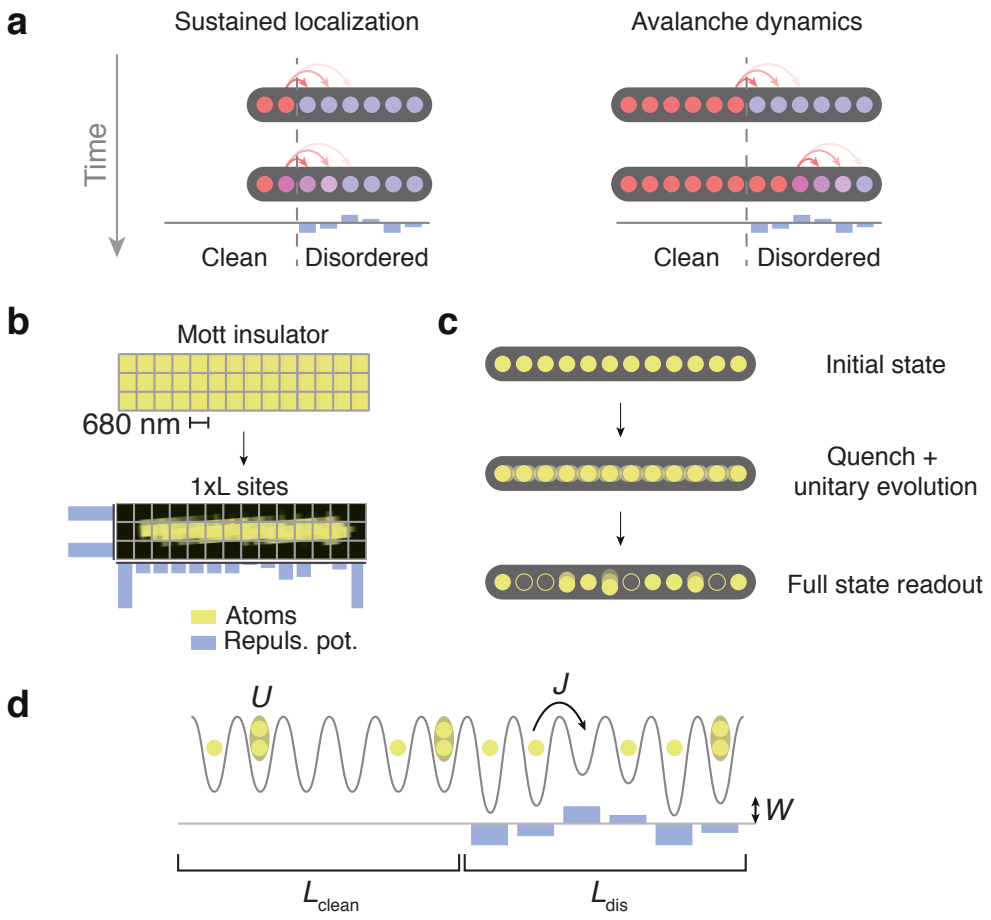

Fig. 10: ***Bath-induced quantum avalanches.*** ***a:*** *Two scenarios at an interface of a thermal bath (clean) and a localized (disordered) region: the bath penetrates logarithmically slow and localization remains robust (left), or an avalanche from a strong bath thermalizes the disordered region site by site (right).* ***b:*** *Fluorescence pictures of a two-dimensional Mott insulator at unity filling, and of the initialized one-dimensional system of L sites. Projected optical potentials isolate the system and apply site-resolved offsets onto the disordered region (blue).* ***c:*** *The initial state is brought far from equilibrium through a quantum quench by abruptly enabling tunneling along all links, then evolved under the Hamiltonian, until we detect the site-resolved atom number with a fluorescence picture.* ***d:*** *The system's dynamics are governed by the Bose-Hubbard model with tunneling energy J and on-site interaction energy U, extended by a disorder potential with amplitude W in the disordered region.*

tunneling rate between neighboring sites. Consequently, within a perturbative description MBL remains robust against a local bath, with a bath penetration into the MBL region that increases logarithmically in time.

Quantum avalanches, in contrast, are predicted to emerge from dynamics beyond this simple picture (Fig. 10a, right). A more accurate description ought to take into account that the density of states of the bath grows when the first disordered site thermalizes and hence merges with the bath. This feedback effect enhances the relaxation rate Γ_i for the next localized sites, giving rise to accelerated bath penetration into the disordered region faster than logarithmic in time. Eventually, these non-perturbative relaxation processes may lead to a full delocalization of the

system if the density of states grows faster than the decay in the coupling rates.
Studying quantum avalanches within disordered systems remains a challenge due to both the statistical rareness of a sufficiently large thermal inclusion, and the large time scales over which the inclusion spreads through the system. Consequently, theoretical approaches often consider disordered systems that are locally coupled to a thermal bath that represents the rare region [68]. Within this canonical setting, several signatures have been proposed to identify quantum avalanches through their short-term dynamics, including a speedup compared to a logarithmic spreading [70], and a backaction on the bath [49]. However, high demands in local control have so far hindered their experimental observation.

4.3 Accelerating delocalization

In this work we explore the dynamics of an MBL system coupled to a thermal inclusion (Fig. 10) and observe phenomena that suggest the presence of non-perturbative avalanche processes. Our experimental protocol starts by preparing a Mott-insulating state with one ^{87}Rb atom on each site of a two-dimensional optical lattice (Fig. 10b). The system is placed in the focus of a high-resolution imaging system through which we project site-resolved repulsive potentials on individual lattice sites. We isolate a one-dimensional system of L lattice sites from the Mott insulator and add potential offsets to the lattice sites. At this point, the system remains in a product state of one atom per lattice site. We then perform a quantum quench by abruptly reducing the lattice depth (Fig. 10c). The subsequent non-equilibrium dynamics are described by the Bose-Hubbard Hamiltonian:

$$\hat{\mathcal{H}} = -J \sum_i \left(\hat{a}_i^\dagger \hat{a}_{i+1} + h.c. \right) + \frac{U}{2} \sum_i \hat{n}_i \left(\hat{n}_i - 1 \right) + W \sum_{i \in L_{\text{dis}}} h_i \hat{n}_i, \tag{3}$$

where $\hat{a}_i^\dagger$ $\left(\hat{a}_i\right)$ is the creation (annihilation) operator for a boson on site i, and $\hat{n}_i = \hat{a}_i^\dagger \hat{a}_i$ is the particle number operator. The first term describes the tunneling between all neighboring lattice sites, and the second term represents the on-site repulsive interactions. The last term introduces a site-resolved energy offset. We set $h_i = 0$ for all lattice sites in the clean region of size L_{clean}, whereas the energy offsets in the disordered region of size L_{dis} follow a quasi-periodic disorder distribution $h_i = \cos(2\pi\beta i + \phi)$ with $1/\beta \approx 1.618$, phase ϕ and amplitude W. The quasi-periodic distribution avoids nearby lattice sites to coincidentally have similar energy offsets, which inhibits the presence of secondary rare regions within the disordered region [55]. After a variable evolution time, we read out the site-resolved atom number by fluorescence imaging. The applied unitary evolution preserves the initial purity of $99.1(2)\%$ per site [8, 1]. All observables are averaged over 200 disorder realizations with different ϕ. The tunneling time $\tau{=}\hbar/J{=}4.3(1)$ ms (with the reduced Planck constant $\hbar$), the interaction strength $U{=}2.87(3)\,J$, and the number of disordered sites $L_{\text{dis}} = 6$ remain constant in all experiments.
We first use the full site-resolved readout of our microscope to investigate the local transport dynamics in the system. The connected density-density correlations $\langle \hat{n}_i \hat{n}_j \rangle_c = \langle \hat{n}_i \hat{n}_j \rangle - \langle \hat{n}_i \rangle \langle \hat{n}_j \rangle$ detect correlations between the particle numbers on site i and j [2]. Negative values of $\langle \hat{n}_i \hat{n}_j \rangle_c$

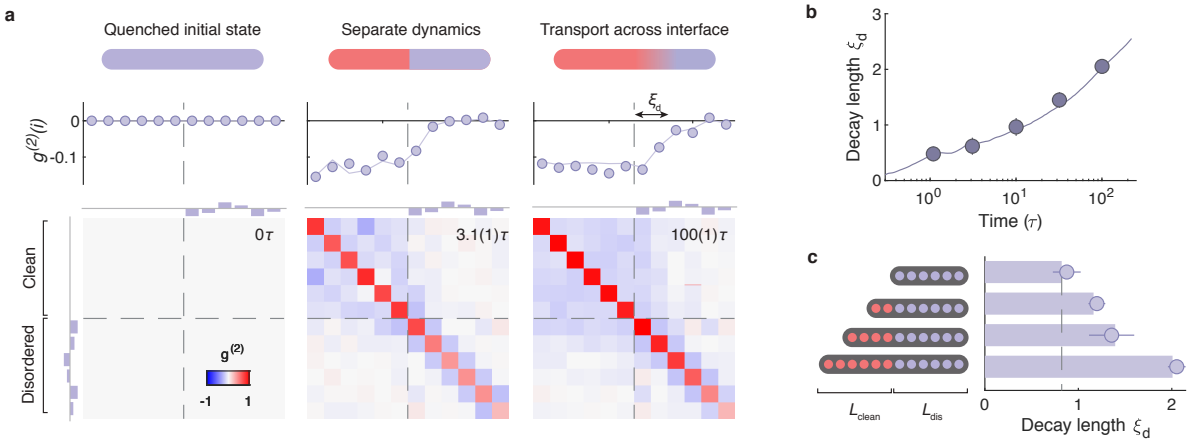

Fig. 11: ***Accelerated transport across the clean-disorder interface. a:*** *Density correlations for all pairs of sites in a system consisting of $L_{clean} = L_{dis} = 6$ at disorder strength $W = 9.1\,J$. After a quantum quench, an uncorrelated initial state (left) develops separate dynamics within each subsystem (center), followed by particle transport across the clean-disorder interface (grey dashed lines) for evolution times $\gg L_{clean}, L_{dis}$ (right). Cuts show the total density correlations $g^{(2)}(i)$ of the clean region with site i (i.e. average of top six rows, excluding diagonal entries), featuring homogeneous coupling among the clean sites, and exponentially decaying anti-correlations with the distance of the disordered site from the interface.* ***b:*** *The decay length ξ_d of the total density correlations increases first logarithmically in time and accelerates at long evolution times.* ***c:*** *The decay length ξ_d after an evolution time of 100τ grows with L_{clean}, indicating improved particle transport into the disordered region. The data point at $L_{clean} = 0$ and the dashed line show the localization length of an isolated MBL system.*

signal anti-correlated density fluctuations, and thus particle motion between the involved sites (Fig. 11a). In the following, we consider a system with $L_{\text{clean}} = 6$ at disorder strength $W = 9.1\,J$ after different evolution times T after the quantum quench. At the beginning of the evolution ($T = 0\tau$), we do not detect any correlations, because the initial state is a product state. After short evolution times ($T \lesssim \tau L$), we observe the buildup of spatially dependent anti-correlations in the system. Within the clean region all lattice sites develop mutual anti-correlations, signaling delocalized particles. In contrast, the anti-correlations in the disordered region remain short-ranged, indicating localized particles. These properties overall persist up to long evolution times ($T \gg \tau L$). In order to quantify the emergence of a bath, we extract the mean and the variation of the off-diagonal correlations in the clean region (Fig. 11b). We find that within a few tunneling times the clean region reaches its steady state with similar correlations across all pairs of sites, indicating that it starts to act as a thermal bath to the disordered region.

For long evolution times ($T \gg \tau L$) we additionally observe the buildup of anti-correlations between lattice sites in the clean and the disordered region, evidence for transport dynamics across the interface (right panel in Fig. 11a). Each of the disordered sites is similarly anti-correlated to all clean sites, which confirms that the clean region acts as a heat bath for the disordered region. Motivated by this picture, we extract the mean correlations of the clean region $g^{(2)}(i) = \overline{\langle \hat{n}_i \hat{n}_j \rangle_c}\big|_{j \in L_{\text{clean}}}$ by averaging the correlations of each site i with all clean sites j

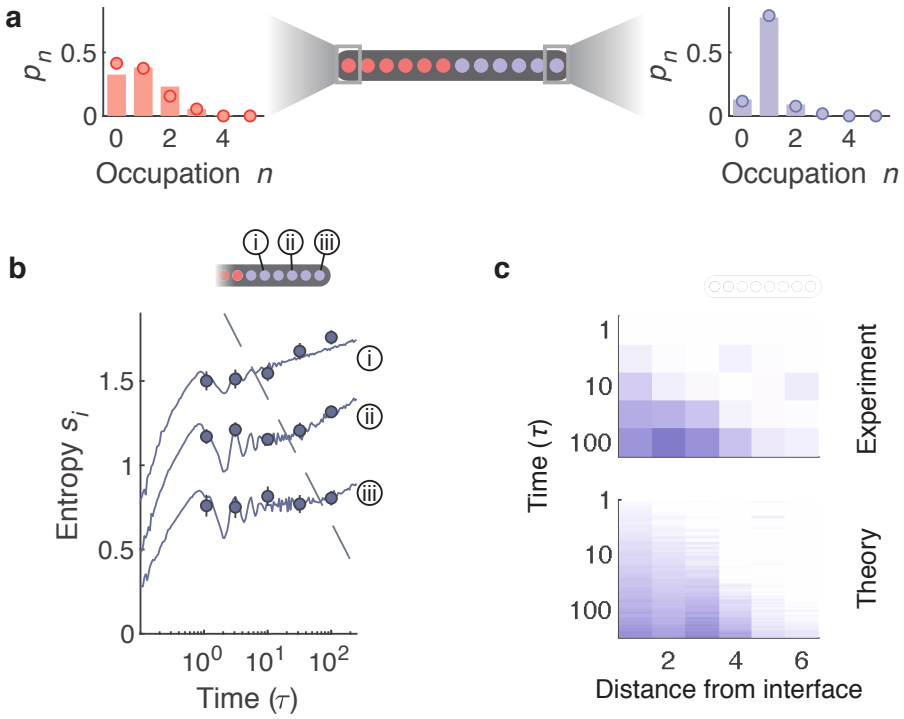

Fig. 12: ***Site-resolved thermalization dynamics.*** ***a:*** *The atom number probability distribution for the edge sites in the clean region (left) and the disordered region (right), measured after* 100τ *in a system consisting of* $L_{clean} = L_{dis} = 6$ *at disorder strength* $W = 9.1\,J$. ***b:*** *Local entropy per particle* $s_i = -\sum_n p_n \log p_n / \langle \hat{n}_i \rangle$ *extracted from the atom number distribution on site* i. *The entropy grows after a stationary evolution whose length depends on the distance from the interface (indicated by the grey dashed line). Traces are vertically offset for better readability.* ***c:*** *Local entropy* s_i *(offset by* $s_i(T = 1\tau)$*) for all disordered sites. Solid lines (bars in panel a) show the prediction from exact numerics without free parameters.*

(Fig. 11a cuts). The results are consistent with an exponential decay with distance from the clean region, in agreement with the Fermi golden rule picture of exponentially decaying couplings between bath and MBL.

While a static bath spectrum causes bath correlations to penetrate MBL logarithmically in time, a signature of the quantum avalanche is an accelerated increase, faster than logarithmically in time. In order to test this picture, we quantify the correlation decay into the disordered region by measuring the average distance $\xi_\mathrm{d} = -\sum_{i \in L_\mathrm{dis}} i\, g^{(2)}(i)$ from the clean region over which anti-correlations form (Fig. 11c). At short times the decay length ξ_d increases logarithmically in time, but accelerates at long evolution times. We contrast this observation with a system with $L_\mathrm{clean} = 2$, where the we do not find any accelerating transport dynamics.

4.4 Site-resolved thermalization

We next examine the local thermalization dynamics across the system. The microscopic readout enables us to measure the full atom number distribution on each site (Fig. 12a). Lattice sites in the clean region show a distribution corresponding to a thermal ensemble, whereas lattice sites

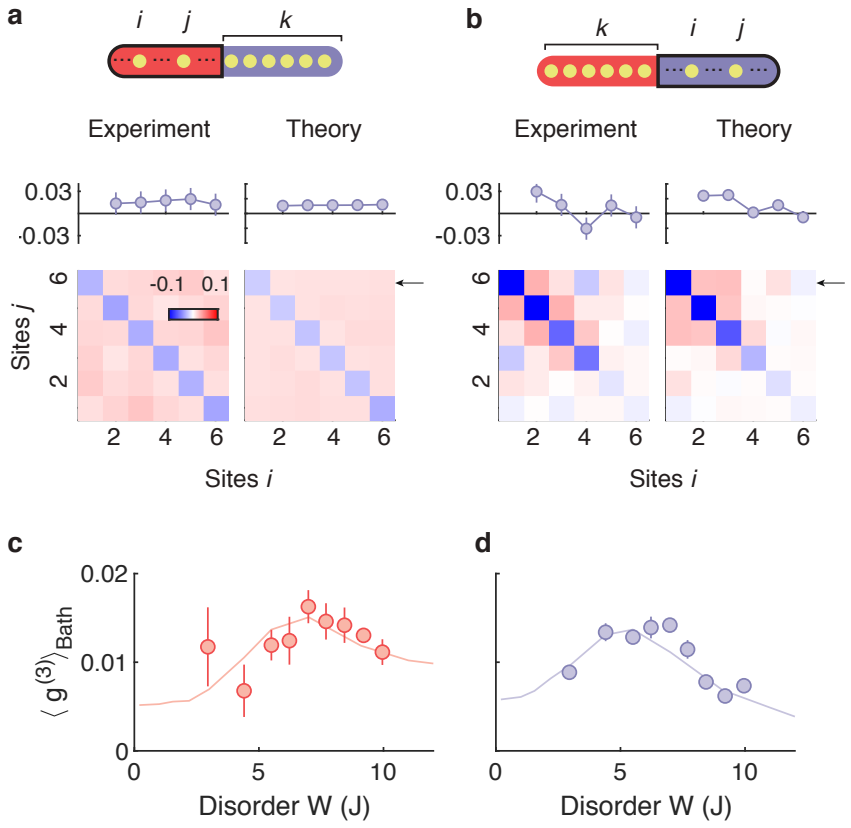

Fig. 13: ***Bath-induced many-body correlations. a:*** *Three-point correlations* $\langle \hat{n}_i \hat{n}_j \hat{n}_k \rangle_c$ *among pairs of clean sites* i, j *and one disordered site* k *(summed over all disordered* k*) in a system with* $L_{clean} = L_{dis} = 6$ *at disorder strength* $W = 9.1\,J$ *and evolution time* $T = 100(1)$*. Cuts across the site* $j = 6$ *(arrows) show nonzero entries for all sites, evidence for multi-particle entanglement between all sites in the clean region with the disordered sites. The flat distribution visualizes the homogeneous coupling to the disordered region.* ***b:*** *Correlations* $\langle \hat{n}_i \hat{n}_j \hat{n}_k \rangle_c$ *among pairs of disordered sites* i, j *and one clean site* k *(summed over all clean* k*) vary strongly with the chosen lattice sites, and decrease with the distance from the clean region. The presence of multi-point correlations demonstrates non-perturbative dynamics: delocalization is driven through many-body processes between the disordered region and the clean region.* ***c:*** *We average over all off-diagonal sites and find a maximum for intermediate disorder for the MBL-bath entanglement.* ***d:*** *The total multi-point correlations among disordered sites with the bath show a similar maximum at slightly lower intermediate disorder. Solid lines show the prediction from exact numerics without free parameters.*

in the disordered region show a distribution with enhanced probability for one particle, the initial state of the system. We quantify the site-resolved thermalization dynamics with the entropy per particle $s_i = -\sum_{n_i} p(n_i) \log p(n_i) / \langle \hat{n}_i \rangle$ on site i from the atom number distributions. We observe reduced thermalization dynamics of the disordered sites with increasing distance from the interface (Fig. 12b, c). Moreover, the data suggest that the dynamics are first stationary until thermalization sets in with a delay that increases with the site's distance from the interface. This picture is confirmed by our exact numerical calculations.

4.5 Many-body processes

The accelerated transport indicates the long-term dynamics are driven by processes that go beyond a perturbative coupling to the bath. We investigate this effect through multipoint correlations [92, 2]. The presence of non-zero three-point connected correlations $\langle \hat{n}_i \hat{n}_j \hat{n}_k \rangle_c$ signals the presence of entanglement among all involved lattice sites, which cannot be explained in a perturbative, semiclassical description. We evaluate the connected correlations $g^{(3)}(i,j) = \overline{\langle \hat{n}_i \hat{n}_j \hat{n}_k \rangle_c}\big|_{k \in L_{\text{clean}}}$ among two disordered sites i, j and a clean site k, averaged over all possible k (Fig. 13a). We find a strong dependence on the involved disordered sites: close to the interface correlations are strong, whereas they become weaker for distant sites. We quantify this behavior by considering the correlations as a function of the mean distance $\bar{d} = (i+j)/2$ of the two disordered sites from the clean region (Fig. 13b). Indeed, the correlations decrease with increasing distance from the clean region, comparable to the decay length ξ_{d}. This demonstrates that the accelerated transport is driven by many-body processes, a key property for quantum avalanches. We quantify the presence of many-body correlations at different disorder strengths by taking their average $\overline{g^{(3)}(i,j)}\big|_{i,j \in L_{\text{dis}}}$ (Fig. 13c,d). The correlations are present throughout the covered disorder range with a maximum at intermediate strengths, close to the estimated critical point of the system [2].

In conclusion, we experimentally realized a clean-disordered interface and studied the emerging thermalization dynamics. We observed an accelerated intrusion of the bath in the MBL system, its evolution to thermal equilibrium site after site, and the many-body correlations between the two subsystems, the hallmarks of quantum avalanches. In future, our experiments can be readily extended in many ways. For example, by increasing both the system size of the disordered region, one could explore the interplay at intermediate disorder strengths in a quantitative way through its scaling behavior, i.e., by increasing the system size at constant ratio of L_{clean} and L_{dis}, which may provide insight into the critical behavior of the transition. An interesting extension would also be the influence of the statistical distribution of the disorder on the critical behavior of the system. Furthermore, engineering other heterostructures with quantum gas microscopes may provide an avenue to studying phenomena in the physics of interfaces, or to building atomtronic devices.

References

[1] A. Lukin, M. Rispoli, R. Schittko, M.E. Tai, A.M. Kaufman, S. Choi, V. Khemani, J. Léonard, and M. Greiner, Science **364**, 256 (2019)

[2] M. Rispoli, A. Lukin, R. Schittko, S. Kim, M.E. Tai, J. Léonard, and M. Greiner, Nature **573**, 385 (2019)

[3] J. Léonard, S. Kim, M. Rispoli, A. Lukin, R. Schittko, J. Kwan, E. Demler, D. Sels, and M. Greiner, Nat. Phys. **19**, 481 (2023)

[4] J.M. Deutsch, Phys. Rev. A **43**, 2046 (1991)

[5] M. Srednicki, Phys. Rev. E **50**, 888 (1994)

[6] M. Rigol, V. Dunjko, and M. Olshanii, Nature **452**, 854 (2008)

[7] C. Neill, P. Roushan, M. Fang, Y. Chen, M. Kolodrubetz, Z. Chen, A. Megrant, R. Barends, B. Campbell, B. Chiaro, A. Dunsworth, E. Jeffrey, J. Kelly, J. Mutus, P.J. O'Malley, C. Quintana, D. Sank, A. Vainsencher, J. Wenner, T.C. White, A. Polkovnikov, and J.M. Martinis, Nat. Phys. **12**, 1037 (2016)

[8] A.M. Kaufman, M.E. Tai, A. Lukin, M. Rispoli, R. Schittko, P.M. Preiss, and M. Greiner, Science **353**, 794 (2016)

[9] R. Nandkishore and D.A. Huse, Annu. Rev. Condens. Matter Phys. **6**, 15 (2015)

[10] P.W. Anderson, Phys. Rev. **109**, 1492 (1958)

[11] T. Schwartz, G. Bartal, S. Fishman, and M. Segev, Nature **446**, 52 (2007)

[12] J. Billy, V. Josse, Z. Zuo, A. Bernard, B. Hambrecht, P. Lugan, D. Clément, L. Sanchez-Palencia, P. Bouyer, and A. Aspect, Nature **453**, 891 (2008)

[13] G. Roati, C. D'Errico, L. Fallani, M. Fattori, C. Fort, M. Zaccanti, G. Modugno, M. Modugno, and M. Inguscio, Nature **453**, 895 (2008)

[14] Y. Lahini, A. Avidan, F. Pozzi, M. Sorel, R. Morandotti, D.N. Christodoulides, and Y. Silberberg, Phys. Rev. Lett. **100**, 013906 (2008)

[15] B. Deissler, M. Zaccanti, G. Roati, C. D'Errico, M. Fattori, M. Modugno, G. Modugno, and M. Inguscio, Nat. Phys. **6**, 354 (2010)

[16] B. Gadway, D. Pertot, J. Reeves, M. Vogt, and D. Schneble, Phys. Rev. Lett. **107**, 1 (2011)

[17] S.S. Kondov, W.R. Mcgehee, J.J. Zirbel, and B. DeMarco, Science **334**, 66 (2011)

[18] F. Jendrzejewski, A. Bernard, K. Müller, P. Cheinet, V. Josse, M. Piraud, L. Pezzé, L. Sanchez-Palencia, A. Aspect, and P. Bouyer, Nat. Phys. **8**, 398 (2012)

[19] C. D'Errico, E. Lucioni, L. Tanzi, L. Gori, G. Roux, I.P. McCulloch, T. Giamarchi, M. Inguscio, and G. Modugno, Phys. Rev. Lett. **113**, 1 (2014)

[20] S.S. Kondov, W.R. McGehee, W. Xu, and B. Demarco, Phys. Rev. Lett. **114**, 1 (2015)

[21] G. Semeghini, M. Landini, P. Castilho, S. Roy, G. Spagnolli, A. Trenkwalder, M. Fattori, M. Inguscio, and G. Modugno, Nat. Phys. **11**, 554 (2015)

[22] I.V. Gornyi, A.D. Mirlin, and D.G. Polyakov, Phys. Rev. Lett. **95**, 206603 (2005)

[23] D.M. Basko, I.L. Aleiner, and B.L. Altshuler, Ann. Phys. **321**, 1126 (2006)

[24] V. Oganesyan and D.A. Huse, Phys Rev. B **75**, 115111 (2007)

[25] E. Altman and R. Vosk, Annu. Rev. Condens. Matter Phys. **6**, 383 (2015)

[26] D.A. Abanin, E. Altman, I. Bloch, and M. Serbyn, Rev. Mod. Phys. **91** (2019)

[27] M. Schreiber, S.S. Hodgman, P. Bordia, H.P. Lüschen, M.H. Fischer, R. Vosk, E. Altman, U. Schneider, and I. Bloch, Science **349**, 842 (2015)

[28] J. Smith, A. Lee, P. Richerme, B. Neyenhuis, P.W. Hess, P. Hauke, M. Heyl, D.A. Huse, and C. Monroe, Nat. Phys. **12**, 907 (2016)

[29] P. Bordia, H.P. Lüschen, S.S. Hodgman, M. Schreiber, I. Bloch, and U. Schneider, Phys. Rev. Lett. **116**, 140401 (2016)

[30] J.-Y. Choi, S. Hild, J. Zeiher, P. Schauß, A. Rubio-abadal, T. Yefsah, V. Khemani, D.A. Huse, I. Bloch, and C. Gross, Science **352**, 1547 (2016)

[31] H.P. Lüschen, P. Bordia, S.S. Hodgman, M. Schreiber, S. Sarkar, A.J. Daley, M.H. Fischer, E. Altman, I. Bloch, and U. Schneider, Phys. Rev. X **7**, 011034 (2017)

[32] P. Bordia, H. Lüschen, U. Schneider, M. Knap, and I. Bloch, Nat. Phys. **13**, 460 (2017)

[33] M. Serbyn, Z. Papić, and D.A. Abanin, Phys. Rev. Lett. **110**, 260601 (2013)

[34] M. Serbyn, Z. Papic, and D.A. Abanin, Phys. Rev. Lett. **111**, 127201 (2013)

[35] D.A. Huse, R. Nandkishore, and V. Oganesyan, Phys. Rev. B **90**, 174202 (2014)

[36] M. Žnidarič, T. Prosen, and P. Prelovšek, Phys. Rev. B **77**, 064426 (2008)

[37] J.H. Bardarson, F. Pollmann, and J.E. Moore, Phys Rev. Lett. **109**, 017202 (2012)

[38] S. Aubry and G. André, Ann. Israel Phys. Soc. **3**, 133 (1980)

[39] S. Iyer, V. Oganesyan, G. Refael, and D.A. Huse, Phys. Rev. B **87**, 134202 (2013)

[40] W.S. Bakr, J.I. Gillen, A. Peng, S. Fölling, and M. Greiner, Nature **462**, 74 (2009)

[41] R. Islam, R. Ma, P.M. Preiss, M. Eric Tai, A. Lukin, M. Rispoli, and M. Greiner, Nature **528**, 77 (2015)

[42] A. Elben, B. Vermersch, M. Dalmonte, J.I. Cirac, and P. Zoller, Phys. Rev. Lett. **120**, 50406 (2017)

[43] R. Vosk, D.A. Huse, and E. Altman, Phys. Rev. X **5**, 031032 (2015)

[44] A.C. Potter, R. Vasseur, and S.A. Parameswaran, Phys. Rev. X **5**, 031033 (2015)

[45] V. Khemani, S.P. Lim, D.N. Sheng, and D.A. Huse, Phys. Rev. X **7**, 021013 (2017)

[46] H.P. Lüschen, P. Bordia, S. Scherg, F. Alet, E. Altman, U. Schneider, and I. Bloch, Phys. Rev. Lett. **119**, 260401 (2017)

[47] K. Agarwal, E. Altman, E. Demler, S. Gopalakrishnan, D.A. Huse, and M. Knap, Ann. Phys. (Berlin) **529**, 1 (2017)

[48] W. De Roeck and F. Huveneers, Phys. Rev. B **95**, 155129 (2017)

[49] R. Nandkishore and S. Gopalakrishnan, Ann. Phys. (Berlin) **529**, 1600181 (2017)

[50] U.C. Täuber, Annu. Rev. Condens. Matter Phys. **8**, 185 (2017)

[51] A. Pal and D.A. Huse,Phys. Rev. B.**82**, 174411 (2010)

[52] L.D. Alessio, Y. Kafri, A. Polkovnikov, and M. Rigol, Adv. Phys. **65**, 239 (2016)

[53] A. Lukin, M. Rispoli, R. Schittko, M.E. Tai, A.M. Kaufman, S. Choi, V. Khemani, J. Léonard, and M. Greiner, (2018)

[54] K. Agarwal, S. Gopalakrishnan, M. Knap, M. Müller, and E. Demler, Phys. Rev. Lett. **114**, 160401 (2015)

[55] F. Setiawan, D.-L. Deng, and J.H. Pixley, Phys. Rev. B **96**, 104205 (2017)

[56] P.T. Dumitrescu, R. Vasseur, and A.C. Potter, Phys. Rev. Lett. **119**, 110604 (2017)

[57] A. Goremykina, R. Vasseur, and M. Serbyn, (2018)

[58] P. Bordia, H. Lüschen, S. Scherg, S. Gopalakrishnan, M. Knap, U. Schneider, and I. Bloch, Phys. Rev. X **7**, 041047 (2017)

[59] D.J. Luitz, N. Laflorencie, and F. Alet, Phys. Rev. B **93**, 060201 (2016)

[60] R. Nandkishore, S. Gopalakrishnan, and D.A. Huse, Phys. Rev. B **90**, 064203 (2014)

[61] E. Lucioni, B. Deissler, L. Tanzi, G. Roati, M. Zaccanti, M. Modugno, M. Larcher, F. Dalfovo, M. Inguscio, and G. Modugno, Phys. Rev. Lett. **106**, 230403 (2011)

[62] H.C. Liu, Phys. Rev. A **94**, 023827 (2016)

[63] T. Schweigler, V. Kasper, S. Erne, I. Mazets, B. Rauer, F. Cataldini, T. Langen, T. Gasenzer, J. Berges, and J. Schmiedmayer, Nature **545**, 323 (2017)

[64] S.S. Hodgman, R.I. Khakimov, A.G. Truscott, and K.V. Kheruntsyan, Phys. Rev. Lett. **118**, 240402 (2017)

[65] T. Grover, arXiv:1405.1471v1 (2014)

[66] F. Alet and N. Laflorencie, Comptes Rendus Phys. **19**, 498 (2018)

[67] D.A. Abanin, E. Altman, I. Bloch, and M. Serbyn, Rev. Mod. Phys. **91**, 021001 (2019)

[68] D.J. Luitz, F. Huveneers, and W. De Roeck, Phys. Rev. Lett. **119**, 150602 (2017)

[69] T. Thiery, F. Huveneers, M. Müller, and W. De Roeck, Phys. Rev. Lett. **121**, 140601 (2018)

[70] P.J. Crowley and A. Chandran, Phys. Rev. Res. **2**, 033262 (2020)

[71] A. Morningstar, L. Colmenarez, V. Khemani, D.J. Luitz, and D.A. Huse, Phys. Rev. B **105**, 174205 (2022)

[72] J. Smith, A. Lee, P. Richerme, B. Neyenhuis, P.W. Hess, P. Hauke, M. Heyl, D.A. Huse, and C. Monroe, Nat. Phys. **12**, 907 (2016)

[73] A. Rubio-Abadal, J.Y. Choi, J. Zeiher, S. Hollerith, J. Rui, I. Bloch, and C. Gross, Phys. Rev. X **9**, 041014 (2019)

[74] D.A. Abanin, J.H. Bardarson, G. De Tomasi, S. Gopalakrishnan, V. Khemani, S.A. Parameswaran, F. Pollmann, A.C. Potter, M. Serbyn, and R. Vasseur, Ann. Phys. **427**, 168415 (2021)

[75] R.K. Panda, A. Scardicchio, M. Schulz, S.R. Taylor, and M. Žnidarič, EPL **128**, 67003 (2019)

[76] P. Sierant, D. Delande, and J. Zakrzewski, Phys. Rev. Lett. **124**, 186601 (2020)

[77] J. Šuntajs, J. Bonča, T. Prosen, and L. Vidmar, Phys. Rev. E **102**, 062144 (2020)

[78] J. Šuntajs, J. Bonča, T. Prosen, and L. Vidmar, Phys. Rev. B **102**, 064207 (2020)

[79] D.J. Luitz and Y.B. Lev, Phys. Rev. B **102**, 100202 (2020)

[80] M. Kiefer-Emmanouilidis, R. Unanyan, M. Fleischhauer, and J. Sirker, Phys. Rev. Lett. **124**, 243601 (2020)

[81] M. Kiefer-Emmanouilidis, R. Unanyan, M. Fleischhauer, and J. Sirker, Phys. Rev. B **103**, 024203 (2021)

[82] D. Sels, Phys. Rev. B **106**, L020202 (2022)

[83] Y. Bar Lev, G. Cohen, and D.R. Reichman, Phys. Rev. Lett. **114**, 100601 (2015)

[84] M. Žnidarič, A. Scardicchio, and V.K. Varma, Phys. Rev. Lett. **117**, 040601 (2016)

[85] S. Gopalakrishnan, K. Agarwal, E.A. Demler, D.A. Huse, and M. Knap, Phys. Rev. B **93**, 134206 (2016)

[86] S. Gopalakrishnan, M. Müller, V. Khemani, M. Knap, E. Demler, and D.A. Huse, Physical Review B **92**, 104202 (2015)

[87] F. Weiner, F. Evers, and S. Bera, Phys. Rev. B **100**, 104204 (2019)

[88] V. Khemani, D.N. Sheng, and D.A. Huse, Phys. Rev. Lett. **119**, 075702 (2017)

[89] S.P. Kelly, R. Nandkishore, and J. Marino, Nucl. Phys. B **951**, 114886 (2020)

[90] R.B. Griffiths, Phys. Rev. Lett. **23**, 17 (1969)

[91] B.M. McCoy, Phys. Rev. Lett. **23**, 383 (1969)

[92] R. Kubo, J. Phys. Soc. Jpn. **17**, 1100 (1962)